PAPER • OPEN ACCESS

Heat and particle exhaust in high-performance plasmas in Wendelstein 7-X

To cite this article: Yu Gao *et al* 2024 *Nucl. Fusion* **64** 076060

View the article online for updates and enhancements.

Heat and particle exhaust in high-performance plasmas in Wendelstein 7-X

Yu Gao[1,*], Joachim Geiger[1], Marcin W. Jakubowski[1], Arun Pandey[1],
Sergey Bozhenkov[1], Yuhe Feng[1], Michael Endler[1], Jürgen Baldzuhn[1],
Valeria Perseo[1], Thierry Kremeyer[1], Georg Schlisio[1], Aleix Puig Sitjes[1],
Matthias Otte[1], Dirk Naujoks[1], Maciej Krychowiak[1], Ralf König[1], Daihong Zhang[1],
Tamás Szepesi[2], Gábor Kocsis[2], Gábor Cseh[2], Attila Buzás[2], Fabio Pisano[3],
Alexander Knieps[4] and the W7-X Team[a]

[1] Max-Planck-Institut für Plasmaphysik, 17491 Greifswald, Germany
[2] Centre for Energy Research, 1121 Budapest, Hungary
[3] University of Cagliari, Department of Electrical and Electronic Engineering, 09123 Cagliari, Italy
[4] Forschungszentrum Jülich GmbH, Institut für Energie- und Klimaforschung—Plasmaphysik, Partner of the Trilateral Euregio Cluster (TEC), 52425 Jülich, Germany

E-mail: yu.gao@ipp.mpg.de

Abstract
The paper reports for the first time the heat and particle exhaust at the plasma boundary through various edge diagnostics for the high-performance plasma obtained after pellet injection on Wendelstein 7-X. The plasma density at the edge is found to be reduced by a factor of 2 in the high-performance phase, supporting the previously reported density peaking at the plasma centre. The plasma beta effect on the magnetic topology is reflected by the appearance of the second strike line, which is well understood with simulation. However, during the rapid decay phase of the enhanced confinement, a transient localized heat flow of up to $16\,\mathrm{MW\,m^{-2}}$ is observed at the leading edge of a poorly cooled divertor component, which has not been understood but raises concerns about machine safety.

Keywords: W7-X, high performance, exhaust

(Some figures may appear in colour only in the online journal)

1. Introduction

In the first divertor campaign on Wendelstein 7-X (W7-X) [1–4], a spontaneous but transient increase of the global energy confinement time τ_E exceeding the empirical ISS04-scaling was observed after the injections of frozen hydrogen pellets [5–8]. The highest volume averaged plasma beta $\langle \beta \rangle$ of $\sim 1\%$ was also achieved in such post-pellet phases with measured diamagnetic energies above 1 MJ. A reduction of turbulence led by strong density peaking was considered to be the main reason for such a transition to high-performance plasmas [5, 7–9]. While the record triple product is obtained in the post-pellet phase, the duration of this enhanced performance was limited to only a few hundred milliseconds and was terminated by a fast-decay of the confined energy, for which the reason is not fully understood. Recent studies suggest that subdominant kinetic ballooning modes may promote increased transport driven by ion temperature gradient as plasma β is raised [10, 11].

Heat and particle exhaust in W7-X is governed by the island divertor [12, 13]. Plasma lost from the confined region is guided by the open field lines inside the helical island chains at the boundary until they intersect with the plasma-facing components (PFCs). According to periodicity and stellarator-symmetry (a flip-symmetry in one period), ten divertor units are distributed toroidally with five in the upper and five in the lower part of the machine [14, figure 1 therein]. The intrinsic 3D magnetic topology at the edge leads to a higher level of complexity in the scrape-off layer physics than that in the tokamak [15], including the investigated toroidal plasma current [16] and beta effects [17], particle drifts [18], counter-streaming flows [19] and transport in the shadowed region [20]. While steady-state power detachment has been demonstrated successfully in various experimental conditions [21], the heat and particle exhaust in the above-mentioned high-performance plasma has not been investigated in detail.

The paper is structured in the following sections. In section 2, the overview of a typical high-performance discharge will be presented. Afterward, the particle exhaust will be analyzed in detail with the measurement from divertor Langmuir probes (LPs) and various video diagnostics. A comparison of plasma beta effects on the power load between simulation and experimental results will be presented in section 4. Furthermore, the up-down and toroidal asymmetries of the power deposition during the fast-decay event will be shown. Finally, we conclude with a summary of the obtained results.

2. Discharge overview

The enhanced confinement after pellet fueling has been well observed experimentally in various magnetic configurations including standard (boundary $n/m = 5/5$, where n and m are toroidal and poloidal mode numbers respectively), high-iota (5/4), and low-iota (5/6) magnetic configurations [6]. The overview plot for one typical high-performance discharge in
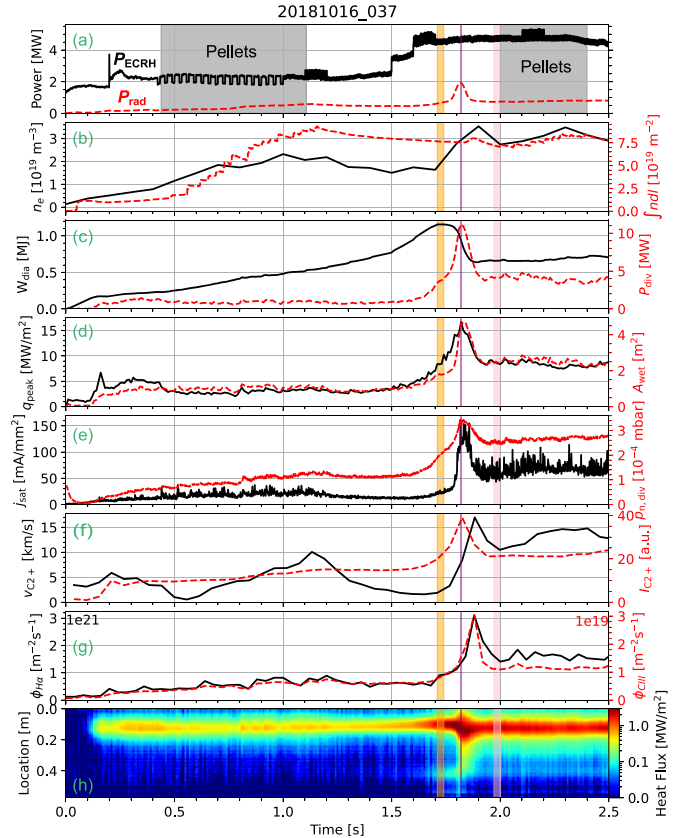
Figure 1. Overview of a high-performance discharge with measurements including various edge diagnostics. The high-beta, the fast-decay, and the low-beta phases are marked in orange, purple, and pink, respectively. (*a*) ECRH heating power P_{ECRH} in solid black line and the total plasma radiation P_{rad} measured by bolometers in dashed red line. (*b*) The edge electron density estimated from a Thomson scattering volume inside the LCFS [42, 43] and the line-integrated electron density $\int n \, dl$ by the interferometer [44]. (*c*) The diamagnetic energy W_{dia} by diamagnetic loop and the total divertor power load P_{div} extrapolated from 8 divertor modules in modules 1 to 4 by infrared thermography. (*d*) The divertor peak heat flux q_{peak} among all the 8 analyzed divertor modules and the calculated total wetted area A_{wet}. (*e*) The divertor ion saturation current j_{sat} measured and averaged over 10 upper and 10 lower divertor LPs in module 5, and the divertor neutral pressure $P_{n,div}$ averaged from the three pressure gauges close to the divertor pumping gap (AEI30, AEI50, and AEI51) [28]. (*f*) The C^{2+} flow velocity V_{C2+} measured by CIS at the same ROI as shown in [19, figure 1(*b*) therein] and the C^{2+} intensity I_{C2+} averaged over the full camera sensor. (*g*) The total photon flux for H_α (in black) and C-III (in red) radiation integrated over all the PFCs captured by available spectroscopic cameras and extrapolated to 10 divertor modules. H_α photon flux is derived from 8 cameras from machine modules 1 to 4, while C-III is derived from one camera monitoring at module 1 lower divertor. (*h*) The averaged heat flux profile over all the divertor elements at the lower iota part for machine modules 1 to 4. Location 0 is defined as the pumping gap end of the target.

standard magnetic configuration is shown in figure 1. Three time periods are investigated in detail: time range 1.71 s to 1.74 s the high-beta phase with $\langle \beta \rangle$ of $\sim 1\%$, 1.82 s the fast-decay event, and 1.97 s to 2.0 s, the low-beta phase with $\langle \beta \rangle$ of $\sim 0.6\%$. Here the plasma volume averaged beta is simply

estimated as $\langle\beta\rangle = \frac{2\mu_0 P}{B^2} \approx \frac{4\mu_0 W_{\text{dia}}}{3B^2 V}$, where μ_0 is the vacuum magnetic permeability constant, P the average plasma pressure, W_{dia} the measured diamagnetic energy, B the magnetic field strength (2.52 T for this discharge), V the plasma volume (30 m^3 in W7-X).

The plasma is heated solely by electron cyclotron resonance heating (ECRH) with a step-like increase of heating power from 2 MW to about 5 MW and remains constant for the labelled three time periods. The plasma radiated power is kept to be low (<1 MW), except for the sharp burst induced by the fast-decay event. Similarly, the toroidal plasma current is rather small and is ignored in the simulation of plasma beta effects in section 4. During the first pellet injection phase from $\sim$0.4 s to $\sim$1.1 s, the line integrated electron density $\int n \mathrm{d}l$ increases from $\sim$1.1 $\times 10^{19}$ m^2 to $\sim$8.8 $\times 10^{19}$ m^2 due to the efficient core fuelling. A slight drop of $\int n \mathrm{d}l$ is observed in the post-pellet phase but remained at a high level above 7.2×10^{19} m^2. The edge electron density estimated from a Thomson scattering volume inside the last closed flux surface (LCFS) is also presented in figure 1(*b*). In contrast to $\int n \mathrm{d}l$, an increase in edge density is observed after the high-beta phase. Details comparing the edge plasma parameters between both beta phases will be presented in section 4.

The increase of the diamagnetic energy (W_{dia}) is not only during the pellet injection phase but also after that. Such spontaneous increase of W_{dia} associated with the increase of energy confinement time was linked to a density peaking with a resulting reduction of turbulence transport [5]. However, the maximum W_{dia} of $\sim$1.15 MJ lasts only $\sim$200 ms, and ends with a fast loss of energy of $\sim$45% within $\sim$50 ms. This amount of energy escaping from the separatrix is mainly deposited onto the 10 divertor modules as measured from the wide-angle infrared thermography [14, 22–24], with the field of view covering all divertor targets. Only $\sim$10% of this fast energy loss is dissipated by plasma radiation measured by the bolometers [25]. The induced peak heat flux (q_{peak}) on the target due to the event is $\sim$16 MW m^{-2}. The total divertor wetted area (A_{wet}) is calculated by integrating the integral power decay length on each divertor element [26]. An increase of A_{wet} of $\sim$40% is found in the low-beta phase over that in the high-beta phase, which corresponds to a narrower main strike line observed in the high-beta phase.

The averaged divertor ion saturation current j_{sat} measured by LPs [27] shows the disappearance of the 'noise' after the end of the pellet injection phase at $\sim$1.2 s. This 'noise' feature re-occurs after the fast-decay event, with the signal baseline doubled, indicating an increased particle flux at the edge. A detailed understanding of the j_{sat} measurement, especially its correlation with the strike line location will be presented in section 3.1. The averaged divertor neutral pressure at the pumping gap ($P_{\text{n,div}}$) measured by pressure gauges [28] shows an increase of $\sim$20% in the low-beta phase compared with the high-beta phase. During the fast-decay event, both measurements suggest an expulsion of particles toward the

divertor, consistent with the heat flux measurement. More details regarding the particle exhaust will be presented in section 3.

Previous studies show that in typical gas-fuelled ECRH-heated attached plasmas, the C^{2+} velocity ($V_{\text{C2+}}$) measured by coherence imaging spectroscopy (CIS) has a strong dependence on the line-averaged electron density [19]. However, this is not the case in this pellet-induced high-performance plasma, where the $V_{\text{C2+}}$ is increased by a factor of $\sim$6 in the low-beta phase compared to the high-beta phase, despite an even decreased line-averaged density. One possible explanation for this observation may be the generally enhanced particle transport leading to a higher plasma density at the edge in the low-beta phase, and $V_{\text{C2+}}$ is more linked to the edge density rather than the line-averaged one. The C^{2+} intensity is correlated closely with the total plasma radiation. Interestingly, the intensity and the velocity of C^{2+} peak at different times, although they are derived from the same camera. A delay of $\sim$60 ms is found in the velocity signal of C^{2+}. Such delay of peaking is also observed in the H_α and C-III radiation obtained from multiple spectroscopic cameras [29]. The reason for this delay is currently not clear. However, the peak of the edge density is also observed to be delayed relative to the fast-decay event, as illustrated in figure 1(*b*). This suggests a correlation between these edge spectroscopic measurements and the edge density. While the C-III radiation is slightly higher in the low-beta than in the high-beta phase, the H_α radiation is enhanced by 100%, which is in agreement with the j_{sat} measurement. Due to the low camera frame rate of 25 Hz, the H_α cameras are not fast enough to capture the fluctuations as has been shown in the j_{sat} signal.

The time evolution of the averaged heat flux profile on the horizontal target is shown in figure 1(*h*). The location of the pumping gap is defined as location 0. A narrower strike line is observed after the pellet injection phase after $\sim$1.2 s, which seems to be correlated with the 'noise-free' behaviour of j_{sat}. The strike line location effect on the j_{sat} measurement will be detailed in section 3.1. A clear difference between the high and the low-beta phases can be summarized as follows: In the high-beta phase, the strike line is obviously much narrower compared with the low-beta phase. Furthermore, a second strike line can be observed at a distance of $\sim$0.4 m from the pumping gap during the high-beta phase, which becomes weaker but is still visible in the log-scale colorbar in the low-beta phase. Thirdly, the location of the main strike line is closer to the pumping gap in the high-beta phase, which is in general beneficial for a higher $P_{\text{n,div}}$ [30, 31]. Thus, the actual measured lower $P_{\text{n,div}}$ in the high-beta phase can only be attributed to a much lower plasma density at the vicinity of the divertor. Finally, a significantly broader and stronger heat load appears at the fast-decay event, in line with the described larger values of A_{wet} and q_{peak}. More details on the understanding of heat transport will be presented in section 4.

3. Particle exhaust

It is clear from the previous section that a reduced level of particle flux to the divertor by a factor of 2 is measured during the high-performance phase, both from the divertor LPs and the H_α spectroscopic cameras. However, we investigate these measurements further in detail in this section, regarding the potential influence of the strike line movement on the j_{sat} measurement and also the effect of the second strike line on the particle exhaust. A broader deposition area during the fast-decay event is observed and will also be presented in this section.

3.1. LP measurement

In the W7-X Operation Phase 1.2, 20 graphite facetted flush-mounted LPs [27] are installed in identical locations in the two divertor modules placed in the machine modules 5 upper and 5 lower. More specifically, they are located in the target module 3, element numbers 3 and 4 (TM3h3, TM3h4), forming two columns along the respective target element. In this discharge, only the data measured by LPs at TM3h3 are available and therefore used. In figure 2(*a*) the heat flux map (non-area-preserving projection developed in [14]) averaged over the time window of the high-beta phase on divertor module 5 upper is shown, where the LP tips are visible but rendered with artificial heat flux values due to the uncertainty on the emissivity of the probe tips. The second strike line can barely be seen here. Notice that the better visibility of the second strike line in figure 1(*h*) is due to the reduced noise level by the averaging of target elements and divertor modules. Due to this processing of the data, the remaining error field effects [32, 33] on the toroidal asymmetric heat distribution are also compensated.

To investigate the strike line movement effect on the j_{sat} measurement, we take a closer look at both the heat flux profile and the 10 j_{sat} measurements at the divertor element TM3h3 as shown in figure 2(*b*). Here, the main error sources of the j_{sat} measurements are the scatter in the data caused by plasma fluctuations. Due to the beta effect (details see section 4), the strike line on the whole low-iota part of the target is typically closer to the pumping gap by ∼3 cm in the high-beta phase than in the low-beta phase. Such movement adds doubts in a direct comparison of the j_{sat} measurements in the different phases, as most of the LPs are located closer to the strike line in the low-beta phase. As a result, it becomes unclear if the measured high j_{sat} in the low-beta phase is due to the higher particle exhaust or purely to the island separatrix being closer to the LPs. To disentangle this effect, we deliberately adjusted the LP measurements and their corresponding strike line profile on the divertor element TM3h3 during the low-beta phase, shifting them towards the pumping gap by ∼2.5 cm, as illustrated in figure 2(*c*). This manipulation ensured alignment of the peak locations of the strike line profiles across both beta phases. While j_{sat} in both beta phases exhibit a similar trend of exponential decay, the magnitudes in the high-beta phase are

between 40%–60% of those observed in the low-beta phase. It is noteworthy that the three probes situated farthest from the pumping gap at a distance of ∼0.4 m are influenced geometrically by the second leg of the island due to the beta effects, where additional particle influx is anticipated in the high beta phase (detailed explanation see section 4). We can conclude from the above analysis that the global particle exhaust is reduced by ∼50% in the high-beta phase regardless of the geometric effect of the strike line.

In figure 2(*c*), we examine the temporal evolution of different probes. During the low-beta phase, considerable fluctuations are observed in the probe nearest to the strike line (LP_10), while the neighboring probe (LP_09) positioned just ∼2.5 cm away shows much less fluctuation. The j_{sat} signal averaged from both LP_04 and LP_05 shows a rather mitigated fluctuation for both beta phases. As a result, the averaged j_{sat} signal from all LPs (also plotted in figure 1(*e*)) is notably influenced by LP_10 due to its strongly enhanced fluctuations.

To quantify the fluctuation level of the j_{sat} signal, the relative standard deviation (Rstd) is calculated, where the standard deviation of j_{sat} during each phase is divided by its mean value. Rstd facilitates the comparison of fluctuation levels accounting for variations in the baseline value of j_{sat} resulting from different magnitudes of particle influx to each LP. The Rstd of LP_10 is rather prominent in the low beta phase, whereas all other probes exhibit significantly lower Rstd values across both beta phases. As depicted in figure 2(*c*), LP_10 resides at the periphery of the peaking region of the strike line during the low-beta phase. This positioning not only leads to a higher j_{sat}, but also yields an increase of Rstd by approximately a factor of 4. Consequently, it can be inferred that the fluctuations in the j_{sat} measurement primarily stem from particle transport along the main heat channel (separatrix) from the upstream towards the divertor. Conversely, fluctuations in j_{sat} remain comparatively minor in the remote divertor regions, away from the pumping gap. This is consistent with previous studies that filaments in W7-X are primarily confined to their respective flux surfaces and do not exhibit ballistic radial motion [34].

3.2. Spectroscopic and visible camera measurements

For the defined high-beta, fast-decay, and low-beta phases, spectroscopic and visible cameras provide direct insights into the particle exhaust. In figure 3 narrower H_α radiation belts close to the pumping gap and globally reduced radiation intensity on the targets are observed in the high-beta phase compared with the low-beta phase, which reflects the mitigated main ion flux in the high-beta phase as discussed in previous sections. The appearance of the second radiation belt is also clearly visible in the remote area away from the pumping gap. This second radiation belt suggests a second channel for particle exhaust in the high-beta phase. Further confirmation for this is found in the image captured by a visible camera that a clear narrow second radiation belt appears during the high-beta phase, indicating plasma-wall interaction at this location rather remote from the pumping gap.
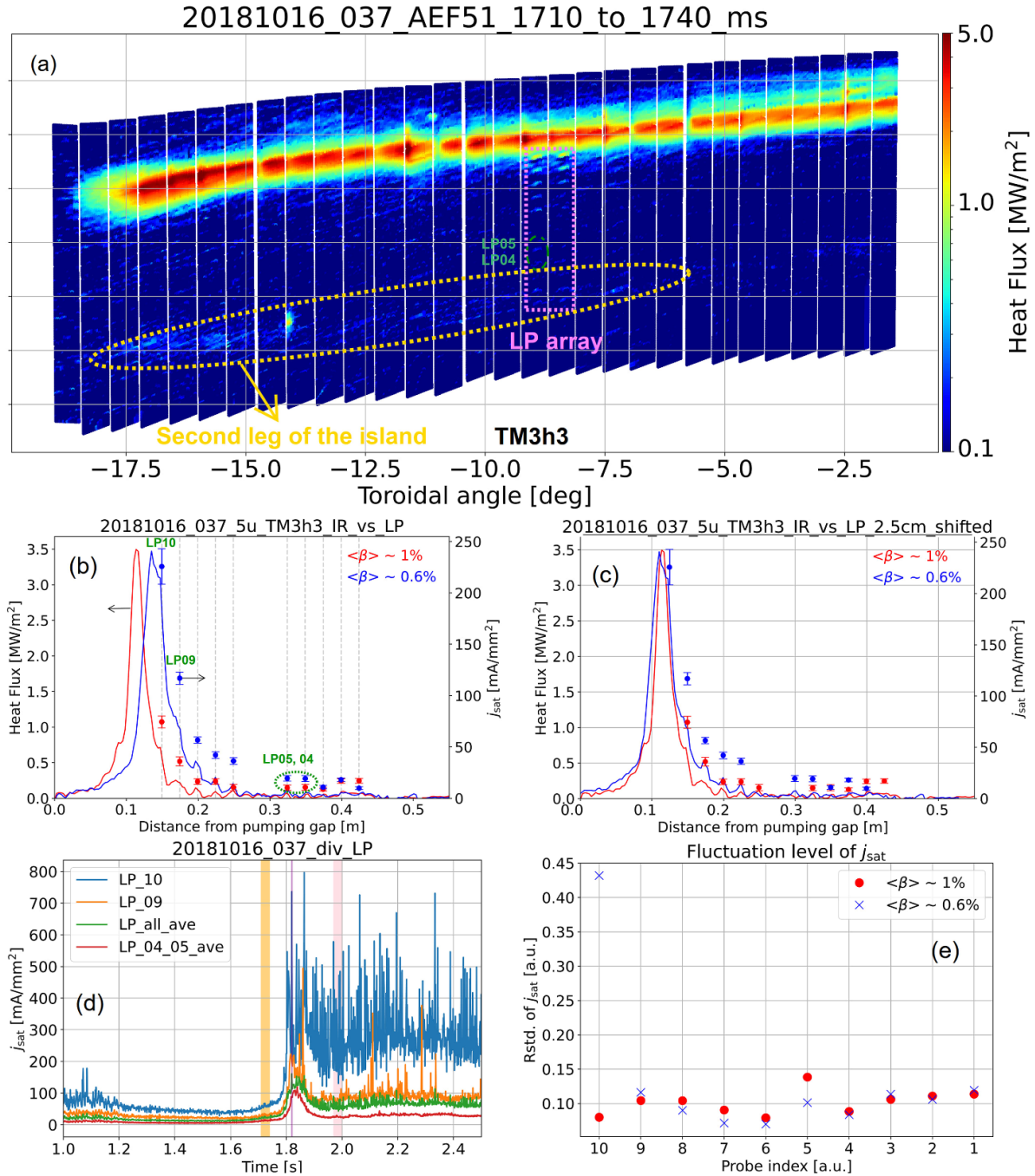
Figure 2. Demonstration of the strike line movement effect on j_{sat} measurements. (*a*) The heat flux map on the low-iota part of divertor module 5 upper averaged over the high-beta phase, where LP arrays are located within the region marked by a purple dotted line, target element TM3h3 in black arrow, and the location of the second strike line in yellow dotted line. The locations of LP_05 and LP_04 are indicated in green. (*b*) The heat flux profile on TM3h3 for both the high-beta (red) and the low-beta phases (blue), as well as the corresponding j_{sat} measurements in dots with the estimated error bar. Locations of LP 10, 9, 5, and 4 are indicated and used for the analysis in (*d*). (*c*) The low-beta measurements in (*b*) are shifted towards the pumping gap by ∼2.5 cm. (*d*) The comparison of j_{sat} by averaging the signals measured from the 2 LP_10 (blue), from the 2 LP_09 (orange), from all the 20 LPs at TM3h3 (green), and from all the 4 LP04 and LP05 probes (red) in both module 5 upper and lower. The high-beta, the fast-decay, and the low-beta phases are indicated in the same color as shown in figure 1. (*e*) The relative standard deviation of the j_{sat} for all the LPs and for both the high-beta (red dots) and the low-beta (blue cross) cases.

At the fast-decay event, both H_α and the visible camera show strong radiation intensity with a broader radiating area. The strong photon flux actually saturates the visible camera at the moment of the fast event. Nevertheless, a speck of bright

dust is observed to flake off and fly away from the outside edge of the horizontal target as shown in figure 3(*f*). This area is typically not loaded by hot plasma in the vacuum standard magnetic configuration. However, it must have received
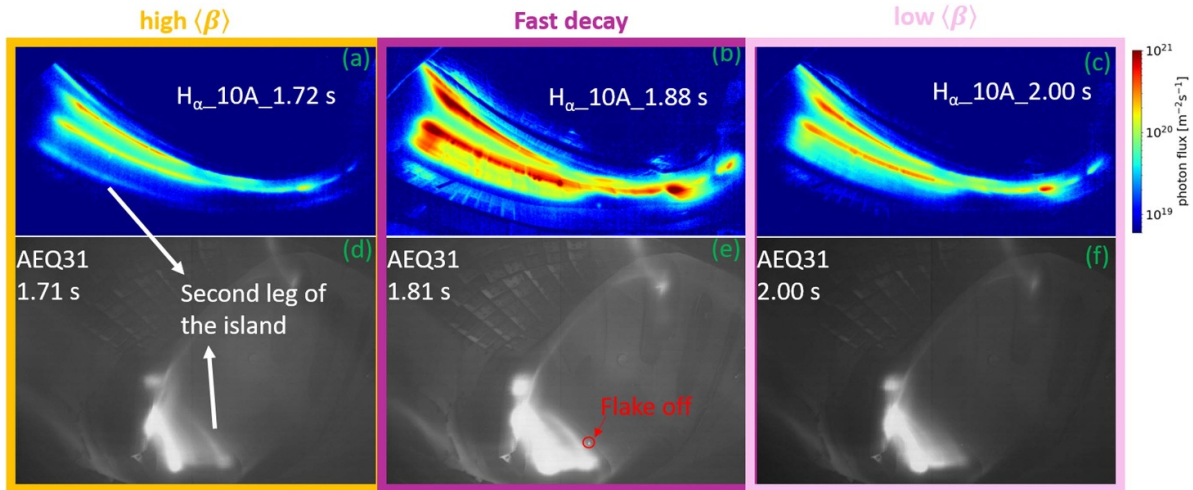
Figure 3. Measurements from different video diagnostics during the high-beta phase (left column), the fast-decay phase (middle column), and the low-beta event (right column). (*a*)–(*c*) Total photon flux obtained from H_α camera monitoring divertor module 1 lower targets. (*d*)–(*f*) One of the visible cameras (AEQ31) tangentially monitoring part of the vertical target and low iota part of the horizontal target in module 4 lower.

much higher heat and particle fluxes by the broader deposition pattern during the fast event. The transient temperature rise at that spot erodes the deposited layer on the surface forming the observed flying dust.

4. Plasma beta effect on the power load

Plasma beta effects on the divertor heat load have been predicted previously with the equilibrium code VMEC + EXTENDER [35] coupled with a simple diffusive field line tracing (DFLT) code [36], where the second strike line has been predicted to be present with $\langle\beta\rangle$ of 2% [37, figure 4.2(*b*) therein]. Due to the missing physics in the simple DFLT [20], an anisotropic diffusion model [38] was proposed and coupled with equilibria calculated with HINT code. This simulation shows again a clear second strike line with central beta β_{ax} of 5% [17, figure 8 therein]. Due to the high-performance phase triggered by the pellet injection in this discharge, it becomes very interesting to verify the prediction with experimental results at $\langle\beta\rangle \sim 1\%$ for the first time. For the heat flux simulation, the EMC3-Lite code [13] is applied here, which includes physics such as a Bohm sheath boundary condition, parallel electron conduction, and perpendicular heat diffusion. This code has been extensively verified with experimental results together with the updated DFLT_rev method and shows good prediction capabilities [31]. The reversible field line mapping technique [39] implemented in the EMC3-Lite reduces the calculation time from hours to minutes compared with the traditional FLT with the same statistical quality. Due to its simplifications (no neutral and impurity interaction), the use of EMC3-Lite code is limited to high power attached conditions, suitable for the investigated high-performance discharge.

Two equilibrium fields are calculated using the VMEC code with $\langle\beta\rangle$ values of $\sim0.6\%$ and $\sim1\%$, respectively, aiming for a good match to the experimental low-beta and high-beta

phases. The fields outside the confined region are produced by the EXTENDER code using a virtual casting principle. Figure 4 shows the wall-to-wall connection length (L_c) overlaid with Poincaré plots at the toroidal angle of $\phi = -15°$ for both plasma-beta cases. The geometric change of the boundary islands is reflected by the modified internal field-line pitch angle (Θ) inside the island [12], such that a global reduction of L_c inside the island by ~100 m is found in the high-beta case. Also, larger islands are formed at the edge in the simulated high-beta case. This leads to an inward shift of LCFS towards the magnetic axis and a displacement of the main strike lines closer to the pumping gap. Theoretically, the increased Θ contributes to a higher ratio of parallel to perpendicular transport for the high-beta phase, which would lead to a narrower strike line width. It is also interesting to see that the second leg of the island (separatrix main heat channel with $L_c > 500$ m) is closer to the divertor with a reduced distance from ~7 cm in the low-beta case to ~3 cm in the high-beta case. The complex geometric change of the island leads to a larger intersection area between the main heat channel and the target in the high-beta phase as shown in figure 5 and as a result, the shadowed area with $L_c < 35$ m between the second strike leg of the island and the target in the poloidal cross-section (shown in figure 4) is reduced. The closer second leg of the island to the divertor target provides higher heat and particle flux to the target directly from the separatrix through perpendicular transport, which explains the observed second strike line and radiation belt seen in the experimental high-beta phase.

The divertor L_c map is compared with the experimental heat flux distribution as shown in figure 5. The location and shape of the divertor strike lines are tightly controlled by the interaction between the main heat channel and the divertor. The rather toroidally extended strike line on the vertical target in the high-beta phase is consistent with the extension of the L_c map. Besides the main strike lines, a segmented toroidal stripe with $L_c \sim 500$ m appears in the middle radial location of
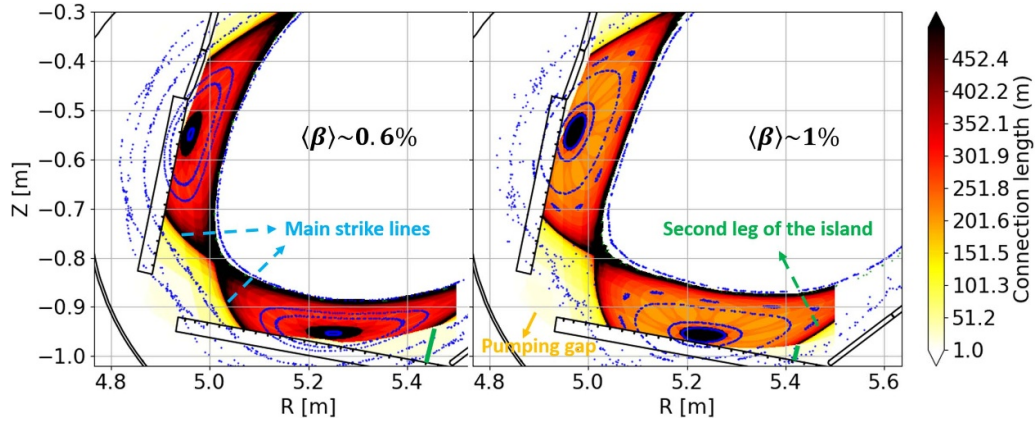
Figure 4. Comparison of connection length overlaid with Poincaré plots at a toroidal angle of $\phi = -15°$ between low and high-beta phases. The second leg of the island is marked by a green dashed arrow, and its distance to the target is also indicated.
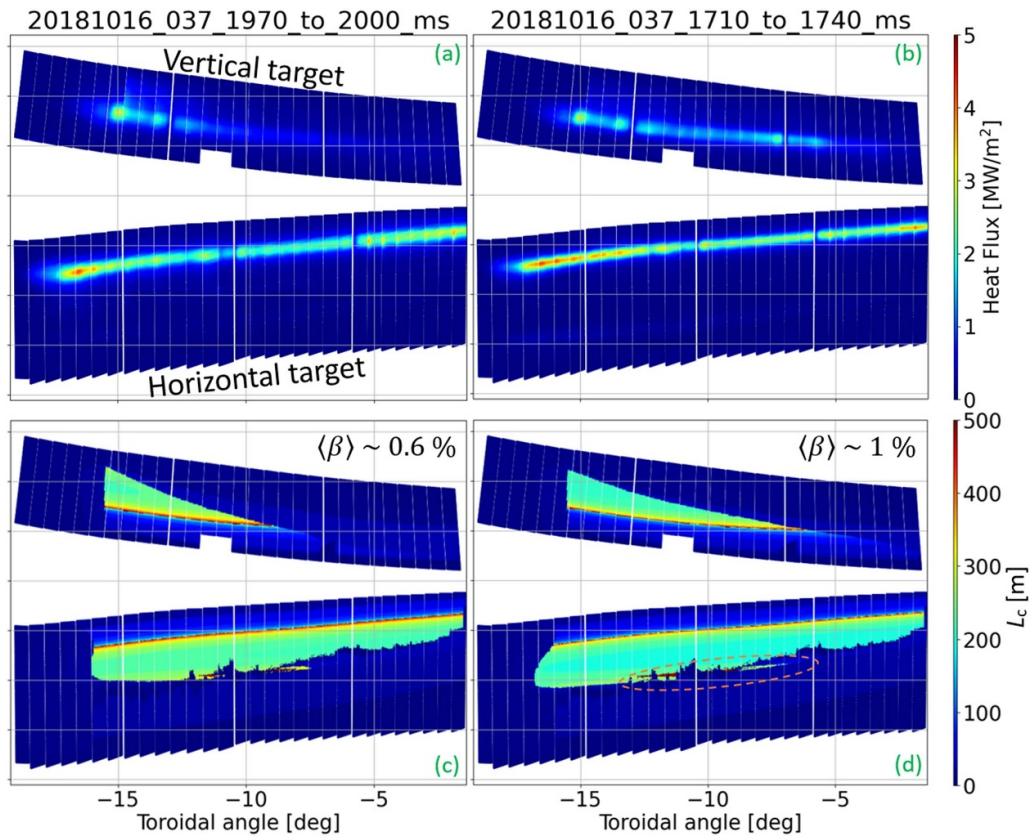

Figure 5. Experimental heat flux map averaged over modules 1–4 ((a), (b)) and the simulated divertor L_c map ((c), (d)). (a), (c) and (b), (d) is for the low-beta, and the high-beta case, respectively. The dashed circle in orange indicates the location of a segmented toroidal stripe with long L_c.

the low iota part for both the high- and low-beta phases. This comes from the intersection of the divertor with the island O point at different toroidal angles as suggested in figure 4. Due to its remote location from the separatrix and dominant parallel heat conduction in this discharge, no hot plasma is found to be deposited via the O point.

To simulate the divertor heat loads, the EMC3-Lite model requires the upstream electron temperature and density as inputs to solve the energy transport equation $\nabla \cdot (-\kappa_e \nabla_\| T - \chi n \nabla_\perp T) = 0$ [13]. For this discharge, Thomson scattering results are properly fitted and mapped to the equilibrium field of the high- and low-beta phases as shown in figure 6 (the region with an effective minor radius $r_{eff} > 0.3$ m is plotted there). Due to the plasma beta effect, the LCFS is shifted inward in the high-beta phase. While the measured electron temperature at the LCFS ($T_{e,LCFS}$) shows a small increase of
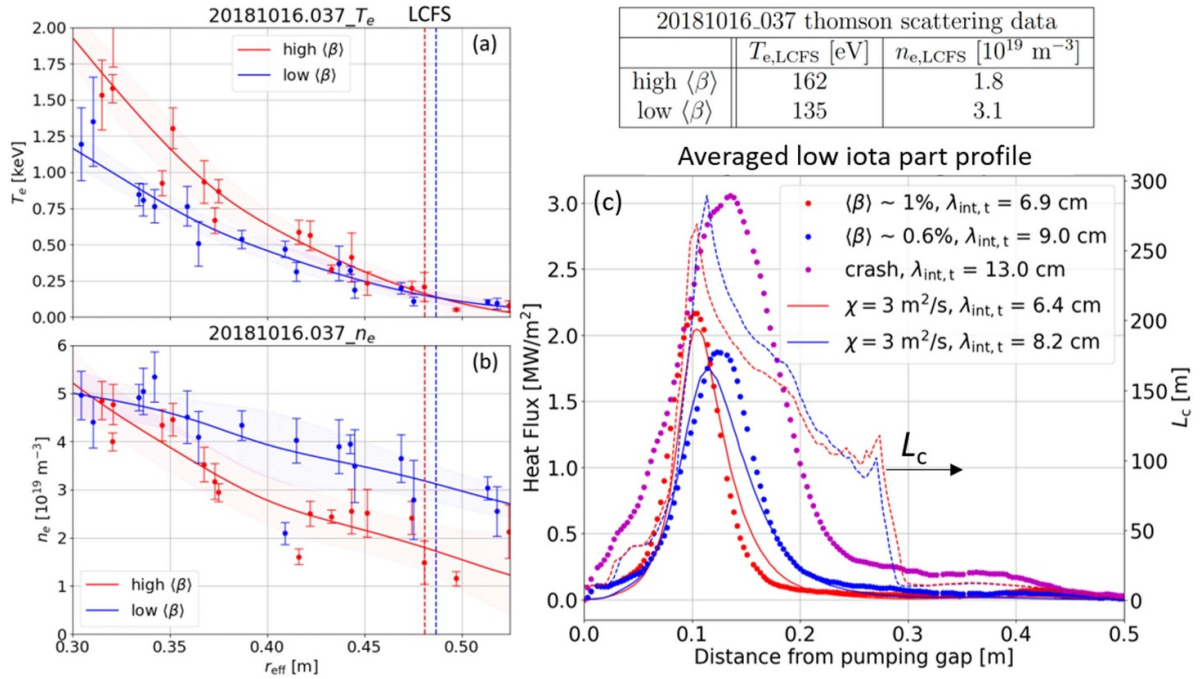
Figure 6. Comparison between the experimental and simulated heat flux profiles. (*a*), (*b*) Electron temperature and density, respectively, measured from Thomson scattering in the high (red) and the low (blue) beta phases (time windows see figure 1). The LCFS positions for both phases are marked by dash lines with respective colors. The upstream parameters used in the EMC3-Lite code are listed in the table. (*c*) The experimental heat flux profile (dots), the simulated heat flux profile (solid curve), and the simulated divertor L_c (dashed curve). All the profiles are averaged over the entire low iota part and, in addition, averaged over modules 1–4 for the experimental results. The integral power decay lengths for different profiles are listed in the legend. The high-beta, the low-beta, and the fast-decay event are marked in red, blue, and purple respectively.

20%, the electron density $n_{e,LCFS}$ is observed to decrease by 40% in the high-beta compared to the low-beta phase. Such a decrease in the upstream density is consistent with the previously shown reduced particle flux on the divertor. The uncertainty of Thomson scattering data is accounted for in the fitting process as shown in figure 6 and is considered to have a rather small influence on the conclusion of the simulation results.

In figure 6(*c*), the experimental and simulated heat flux profiles are compared for the high-beta and the low-beta phases together with simulated divertor L_c. The strike line position is closer to the pumping gap in the high-beta phase as indicated also by the divertor L_c. To quantify the strike line width, the traditionally used integral power decay length defined as $\lambda_{int,t} = \int q(s)\mathrm{d}s/q_{max}$ is calculated for all the profiles. Compared with the low-beta phase, the experimental $\lambda_{int,t}$ shows a decrease of 23% for the high-beta phase, but a substantial increase of 44% during the fast-decay event. Such a broad heat flux profile during the fast event is consistent with the large wetted area and the wide radiation belts described in previous sections. The rather small second peak at ∼0.42 m from the pumping gap is observed for both the simulation and experimental results for the high-beta phase. For the EMC3-Lite simulation, we assume a constant anomalous conductivity in the direction perpendicular to the magnetic field $\chi = \chi_i + \chi_e = 3$ m^2 s^{-1} and found a good agreement with the experimental results. A fine-tuning of χ to get a perfect match is not the purpose of

this study. The same level of χ for both the high and the low-beta phases suggests that the narrower heat flux profile in the high-beta phase is mainly due to the shorter L_c, higher electron temperature, and the lower plasma density both measured at the upstream and the divertor region.

5. Fast-decay event

The fast-decay event has a duration of ∼50 ms for this discharge and terminates the high-performance phase by expelling ∼45% of the confined plasma energy to the PFCs. Although the infrared camera was operated with a limited frame rate of 100 Hz, the rather short exposure time of 5 μs is beneficial to still capture the evolution of the fast event. The obvious difference between the heat distribution on the upper and the lower divertor targets suggests that the strong heat and particle exhaust during the fast event is likely to be coupled with the plasma drifts (see figure 7). The baffle load and the splitting of the main strike lines on both the vertical and horizontal targets only appear on the upper targets. One possible explanation for these loads might be a modified magnetic topology triggered by strong current filaments expelled during the fast event.

The remaining error field is considered to cause toroidal asymmetry of the heat loads in the machine. Such asymmetry seems to be enhanced during the fast events. Figure 7(*c*) shows
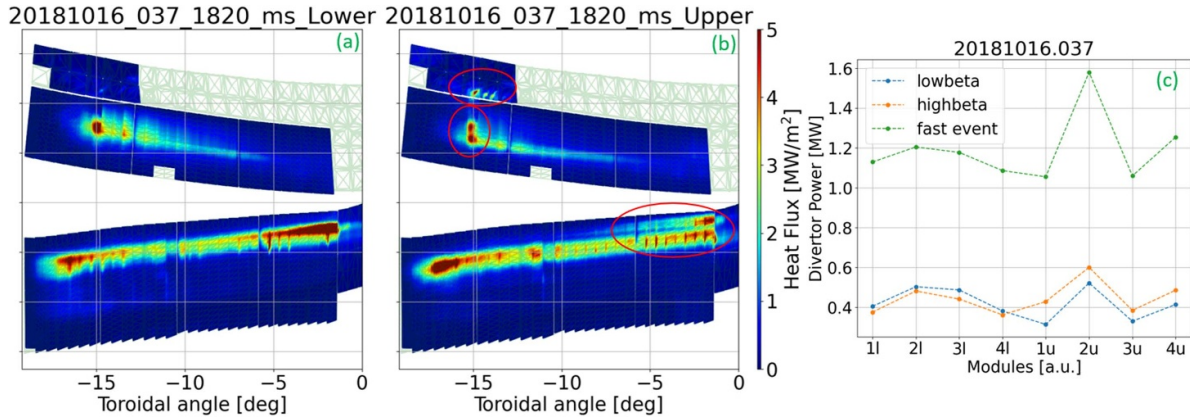
Figure 7. The asymmetries of heat flux distributions due to the particle drifts and the remaining error fields. (*a*), (*b*) The heat flux map during the fast-decay event on the divertor and part of the baffle averaged over all the upper and lower targets in modules 1–4, respectively. (*c*) The divertor total power for each divertor module from 1 to 4 (l for lower, u for upper) for the three phases.
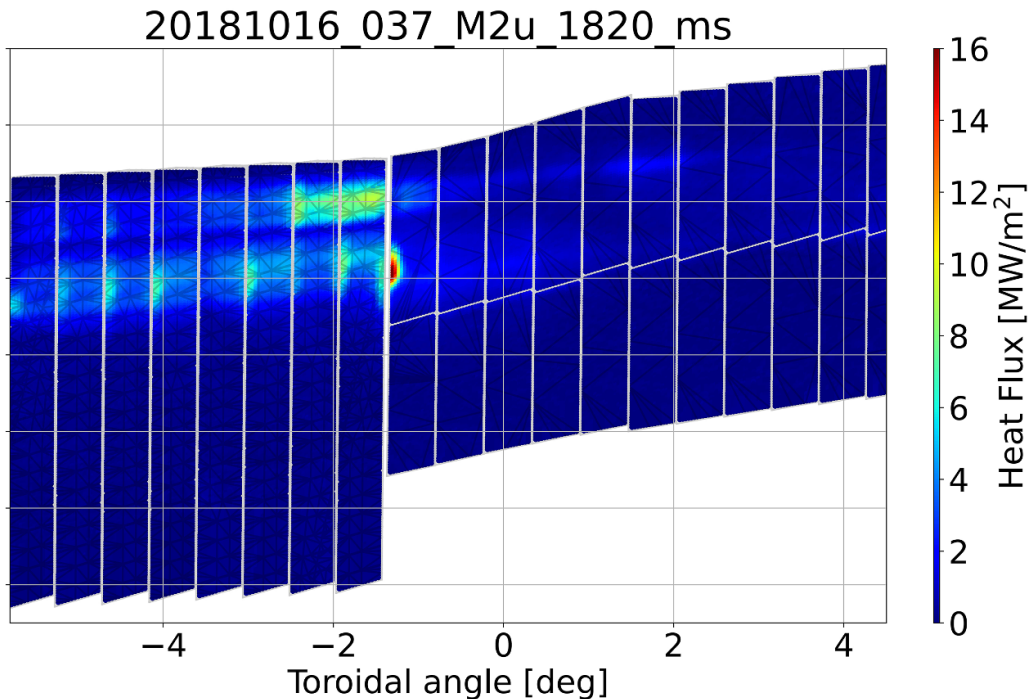

Figure 8. Peak heat load up to $16 \, \mathrm{MW \, m^{-2}}$ during the fast-decay event on divertor module 2 upper horizontal target at the edge of the middle divertor part.

the total divertor loads on the different modules for the three phases. It is clearly seen that the deviation of the total load on module 2 upper (2u) from the others is stronger for the fast event than for the low- and high-beta phases. Such asymmetry seems to be enhanced during the fast event, where the total divertor load on module 2 upper (2u) is increased stronger than that on the other modules, compared with the low and the high-beta phase. In fact, the maximum heat flux of $16 \, \mathrm{MW \, m^{-2}}$ is observed at the leading edge of the middle divertor part in 2u along the main strike line, as shown in figure 8. The middle divertor part is designed to allow for up to $1 \, \mathrm{MW \, m^{-2}}$ steady-state heat flux when water cooling is applied [40]. It has not yet been investigated in detail if such transient high heat fluxes would pose a risk in future operations, especially with

higher heating power. However, it is an interesting physics topic to find an operational scheme compatible with the high-performance discharge and high plasma radiation at the divertor. Impurity seeding is anticipated to keep a high radiation level and a low plasma density at the edge [41], which is beneficial for a peaked density gradient for turbulence reduction.

6. Conclusion

High-performance discharges obtained with pellet injection are of great interest in W7-X. The power and particle exhaust for a typical high-performance discharge is investigated in detail in this paper with various edge diagnostics. The edge

plasma density shows a 50% reduction during the high-performance phase. A second strike line and a radiation belt are observed and can be explained by the beta-changes to the boundary islands. These bring the outer second leg of the island closer to the divertor causing the observations. Simulated heat flux profiles suggest that the narrower strike line in the high-beta phase is mainly due to the shorter connection length, higher electron temperature, and lower plasma density at the edge, rather than a change in the perpendicular heat conductivity. The splitting of the main strike lines and the enhanced baffle loads are also observed, for which the reason is still unknown, but may be linked to a rapid change of magnetic topology. The residual error field appears to augment the localized divertor heat flux at a prominent leading edge, reaching up to 16 MW m^{-2} during the fast event.

Acknowledgments

ORCID iDs

Yu Gao ⬤ https://orcid.org/0000-0001-8576-0970

Marcin W. Jakubowski ⬤ https://orcid.org/0000-0002-6557-3497

Sergey Bozhenkov ⬤ https://orcid.org/0000-0003-4289-3532

Yuhe Feng ⬤ https://orcid.org/0000-0002-3846-4279

Michael Endler ⬤ https://orcid.org/0000-0003-2314-8393

Valeria Perseo ⬤ https://orcid.org/0000-0001-8473-9002

Thierry Kremeyer ⬤ https://orcid.org/0000-0002-6383-944X

Georg Schlisio ⬤ https://orcid.org/0000-0002-5430-0645

Daihong Zhang ⬤ https://orcid.org/0000-0002-5800-4907

Tamás Szepesi ⬤ https://orcid.org/0000-0002-8305-3858

Gábor Cseh ⬤ https://orcid.org/0000-0003-4729-8070

Attila Buzás ⬤ https://orcid.org/0009-0006-1790-5721

Fabio Pisano ⬤ https://orcid.org/0000-0003-0162-0562

Alexander Knieps ⬤ https://orcid.org/0000-0003-0083-7188

References

[1] Pedersen T.S. *et al* 2018 First results from divertor operation in Wendelstein 7-X *Plasma Phys. Control. Fusion* **61** 014035

[2] Klinger T. *et al* 2019 Overview of first Wendelstein 7-X high-performance operation *Nucl. Fusion* **59** 112004

[3] Wolf R.C. *et al* 2019 Performance of Wendelstein 7-X stellarator plasmas during the first divertor operation phase *Phys. Plasmas* **26** 082504

[4] Pedersen T.S. *et al* 2019 First divertor physics studies in Wendelstein 7-X *Nucl. Fusion* **59** 096014

[5] Bozhenkov S. *et al* 2020 High-performance plasmas after pellet injections in Wendelstein 7-X *Nucl. Fusion* **60** 066011

[6] Baldzuhn J. *et al* 2020 Enhanced energy confinement after series of pellets in Wendelstein 7-X *Plasma Phys. Control. Fusion* **62** 055012

[7] Xanthopoulos P. *et al* 2020 Turbulence mechanisms of enhanced performance stellarator plasmas *Phys. Rev. Lett.* **125** 075001

[8] Beurskens M. *et al* 2021 Confinement in electron heated plasmas in Wendelstein 7-X and ASDEX Upgrade; the necessity to control turbulent transport *Nucl. Fusion* **62** 016015

[9] Proll J., Plunk G., Faber B., Görler T., Helander P., McKinney I.J., Pueschel M.J., Smith H.M. and Xanthopoulos P. 2022 Turbulence mitigation in maximum-J stellarators with electron-density gradient *J. Plasma Phys.* **88** 905880112

[10] Mulholland P., Aleynikova K., Faber B.J., Pueschel M., Proll J.,H.,E., Hegna C., Terry P. and Nührenberg C. 2023 Enhanced transport at high plasma pressure and subthreshold kinetic ballooning modes in Wendelstein 7-X *Phys. Rev. Lett.* **131** 185101

[11] Aleynikova K., Zocco A., Xanthopoulos P., Helander P. and Nührenberg C. 2018 Kinetic ballooning modes in tokamaks and stellarators *J. Plasma Phys.* **84** 745840602

[12] Feng Y., Kobayashi M., Lunt T. and Reiter D. 2011 Comparison between stellarator and tokamak divertor transport *Plasma Phys. Control. Fusion* **53** 024009

[13] Feng Y. (W7-X Team) 2022 Review of magnetic islands from the divertor perspective and a simplified heat transport model for the island divertor *Plasma Phys. Control. Fusion* **64** 125012

[14] Gao Y., Jakubowski M.W., Drewelow P., Pisano F., Puig Sitjes A., Niemann H., Ali A. and Cannas B. 2019 Methods for quantitative study of divertor heat loads on W7-X *Nucl. Fusion* **59** 066007

[15] Jakubowski M. *et al* 2021 Overview of the results from divertor experiments with attached and detached plasmas at Wendelstein 7-X and their implications for steady-state operation *Nucl. Fusion* **61** 106003

[16] Gao Y. *et al* 2019 Effects of toroidal plasma current on divertor power depositions on Wendelstein 7-X *Nucl. Fusion* **59** 106015

[17] Knieps A. *et al* 2021 Plasma beta effects on the edge magnetic field structure and divertor heat loads in Wendelstein 7-X high-performance scenarios *Nucl. Fusion* **62** 026011

[18] Hammond K.C. *et al* 2019 Drift effects on W7-X divertor heat and particle fluxes *Plasma Phys. Control. Fusion* **61** 125001

[19] Perseo V. *et al* 2021 2D measurements of parallel counter-streaming flows in the W7-X scrape-off layer for attached and detached plasmas *Nucl. Fusion* **61** 116039

[20] Gao Y. *et al* 2020 Understanding baffle overloads observed in high-mirror configuration on Wendelstein 7-X *Nucl. Fusion* **60** 096012

[21] Feng Y. *et al* 2021 Understanding detachment of the W7-X island divertor *Nucl. Fusion* **61** 086012

[22] Jakubowski M. *et al* 2018 Infrared imaging systems for wall protection in the W7-X stellarator (invited) *Rev. Sci. Instrum.* **89** 10E116

[23] Puig Sitjes A. *et al* 2018 Wendelstein 7-X near real-time image diagnostic system for plasma-facing components protection *Fusion Sci. Technol.* **74** 116

[24] Pisano F., Cannas B., Jakubowski M.W., Niemann H., Puig Sitjes A. and Wurden G.A. 2018 Towards a new image processing system at Wendelstein 7-X: from spatial calibration to characterization of thermal events *Rev. Sci. Instrum.* **89** 123503

[25] Zhang D. *et al* 2010 Design criteria of the bolometer diagnostic for steady-state operation of the W7-X stellarator *Rev. Sci. Instrum.* **81** 10E134

[26] Niemann H. *et al* 2020 Large wetted areas of divertor power loads at Wendelstein 7-X *Nucl. Fusion* **60** 084003

[27] Rudischhauser L. 2021 Langmuir probes in the Wendelstein 7-X test divertor unit *PhD Thesis* Universität Greifswald (available at: https://epub.ub.uni-greifswald.de/frontdoor/index/index/year/2021/docId/5737)

[28] Wenzel U., Schlisio G., Mulsow M., Pedersen T.S., Singer M., Marquardt M., Pilopp D. and Rüter N. 2019 Performance of new crystal cathode pressure gauges for long-pulse operation in the Wendelstein 7-X stellarator *Rev. Sci. Instrum.* **90** 123507

[29] Kremeyer T. *et al* 2022 Analysis of hydrogen fueling, recycling and confinement at Wendelstein 7-X via a single-reservoir particle balance *Nucl. Fusion* **62** 036023

[30] Lazerson S.A. *et al* 2019 Tuning of the rotational transform in Wendelstein 7-X *Nucl. Fusion* **59** 126004

[31] Gao Y. *et al* 2023 Improvement in the simulation tools for heat distribution predictions and control of baffle and middle divertor loads in Wendelstein 7-X *Nucl. Fusion* **63** 026031

[32] Bozhenkov S., Otte M., Biedermann C., Jakubowski M., Lazerson S.A., Sunn Pedersen T. and Wolf R.C. 2018 Measurements and correction of the 1/1 error field in Wendelstein 7-X *Nucl. Fusion* **59** 026004

[33] Lazerson S.A. *et al* 2018 Error fields in the Wendelstein 7-X stellarator *Plasma Phys. Control. Fusion* **60** 124002

[34] Killer C., Shanahan B., Grulke O., Endler M., Hammond K. and Rudischhauser L. 2020 Plasma filaments in the scrape-off layer of Wendelstein 7-X *Plasma Phys. Control. Fusion* **62** 085003

[35] Geiger J. *et al* 2010 Effects of net currents on the magnetic configuration of W7-X *Contrib. Plasma Phys.* **50** 770

[36] Bozhenkov S., Geiger J., Grahl M., Kißlinger J., Werner A. and Wolf R.C. 2013 Service oriented architecture for scientific analysis at W7-X. An example of a field line tracer *Fusion Eng. Des.* **88** 2997

[37] Hölbe H. 2015 Control of the magnetic topology and plasma exhaust in the edge region of Wendelstein 7-X: a numerical study *PhD Thesis* Universität Greifswald (available at: https://epub.ub.uni-greifswald.de/frontdoor/index/index/docId/1642)

[38] Knieps A. *et al* 2022 Anisotropic diffusion as a proxy model for the estimation of heat-loads on plasma-facing components *Plasma Phys. Control. Fusion* **64** 084001

[39] Feng Y., Sardei F. and Kisslinger J. 2005 A simple highly accurate field-line mapping technique for three-dimensional Monte Carlo modeling of plasma edge transport *Phys. Plasmas* **12** 052505

[40] Wang Z., Boscary J. and Schauer F. 2020 Thermal and mechanical analyses of W7-X plasma facing components for operation phase 2 *Fusion Eng. Des.* **161** 111882

[41] Effenberg F. *et al* 2019 First demonstration of radiative power exhaust with impurity seeding in the island divertor at Wendelstein 7-X *Nucl. Fusion* **59** 106020

[42] Pasch E., Beurskens M.N.A., Bozhenkov S.A., Fuchert G., Knauer J. and Wolf R.C. 2016 The Thomson scattering system at Wendelstein 7-X *Rev. Sci. Instrum.* **87** 11E729

[43] Bozhenkov S. *et al* 2017 The Thomson scattering diagnostic at Wendelstein 7-X and its performance in the first operation phase *J. Instrum.* **12** 10004

[44] Brunner K., Akiyama T., Hirsch M., Knauer J., Kornejew P., Kursinski B., Laqua H., Meineke J., Mora H.T. and Wolf R.C. 2018 Real-time dispersion interferometry for density feedback in fusion devices *J. Instrum.* **13** P09002